SHiPA-LLM: Interpretable Regional Crop Production Estimation and Driver Analysis by Coupling Deep Learning with a Knowledge-Grounded Large Language Model

Heyan Di[a,b], Yachao Zhao[a,b], Jiaojiao Tian[c], Xin Du[a,b,*], Qiangzi Li[a,b,*1], Yuan Zhang[a,b], Hongyan Wang[a,b], Jiansong Luo[a,b]

[a]*Aerospace Information Research Institute, Chinese Academy of Sciences, Beijing 100094, China*

[b]*University of Chinese Academy of Sciences, Beijing 100190, China*

[c]*21st Century Space Technology Application Co., Ltd., Beijing 100096, China*

Abstract

Under climate change, regional-scale crop production estimation requires not only stable numerical results, but also a traceable evidence chain that can support mechanism diagnosis and decision-making. Existing regional monitoring systems usually rely on stitching multi-source heterogeneous data with complex alignment procedures, and prediction and explanation are often separated, making it difficult to form an auditable closed loop. Focusing on the main grain-producing region of Northeast China, this study proposes SHiPA-LLM, which couples deep learning estimation with knowledge-constrained large language model interpretation. The framework uses a single Earth observation input, applies a multi-task model to estimate total production and harvested area, derives yield, and reconstructs meteorological variables to form an evidence package. The interpretation module then generates driver explanations based on a knowledge base. Experimental results show that in the regional-scale evaluation over Northeast China, the proposed method achieves R^2=0.7287 and RMSE =43,049.70 kg for production, and R^2=0.7482 and RMSE =19.34 ha for harvested area. We further test the accuracy of physics-derived yield under different thresholds, and at the 90% threshold R^2 reaches 0.63. In addition, the LLM demonstrations show that the framework can provide traceable, evidence-driven explanations for yield variability in anomaly years, offering a practical decision-support path for regional production monitoring and risk assessment.

Keywords: crop production estimation, driver attribution, large language model, physical consistency constraint, retrieval-augmented generation

[1] *Corresponding author: duxin@aircas.ac.cn, liqz@aircas.ac.cn

1 Introduction

Crops are a critical component of the global agricultural economy, providing essential food, feed, and nutritional resources for billions of people (Hartman et al., 2011). Amid growing climate change, geopolitical uncertainties, and supply-chain instability (Sodhi and Tang, 2021), stable crop production has strategic significance for global food security (Giller et al., 2021). However, this stability is increasingly threatened by the rising frequency and intensity of climate extremes, such as heatwaves or droughts during critical growth stages, which introduce significant volatility into crop yield and production (Vogel et al., 2019). Consequently, the key question for large-scale agricultural monitoring is no longer only whether total production or yield can be estimated accurately (Xiong et al., 2024). Instead, it is whether the system can provide both reliable quantitative estimates and mechanism-level driver explanations that are verifiable, traceable, and usable for decision-making under complex uncertainty (Jones et al., 2022). Environmental disturbances and management differences across regions and years create strong spatiotemporal heterogeneity (Qin et al., 2026), which introduces profound uncertainty when numerical results are transferred across scales or generalized across years without explicit and interpretable evidence.

To achieve the dual goals of accurate regional estimation and mechanism explanation, existing remote-sensing methods face a fundamental dilemma between scalability and interpretability. Knowledge-driven crop models (e.g., WOFOST (Van Diepen et al., 1989), APSIM (Keating et al., 2003)) provide excellent mechanistic interpretability, yet they typically rely on numerous field parameters that are difficult to obtain reliably at large regional scales (Kasampalis et al., 2018). Consequently, data-driven models have become the mainstream choice for large-scale monitoring due to their superior scalability and accuracy (Xiong et al., 2024).

However, to capture complex environmental dynamics, these data-driven workflows increasingly rely on fusing multi-source information (e.g., weather, soil, and multispectral remote sensing) (Ma et al., 2021), which inevitably introduces significant bottlenecks in practical applications. Specifically, current data-driven operational workflows struggle with both perception and estimation inefficiencies. On the perception side, the high cost of acquiring, harmonizing, and aligning heterogeneous multi-source data limits deployability and transferability. Such multi-source fusion requires costly spatiotemporal alignment, introduces computational redundancy, and may amplify error propagation (Wang et al., 2018). On the estimation side, regional total production is typically calculated by separately modelling yield and harvested area and then combining them (Ma et al., 2024; Xu et al., 2026). In practice, this decoupled workflow forms a relatively fixed task decomposition and an error propagation path: errors in yield and harvested area accumulate during the synthesis step. When spatial heterogeneity is strong or sample purity is low, the results become highly unstable, which severely affects the reliability of total production at regional and national scales (Stiller et al., 2024). Thus, it is difficult for existing data-driven systems to achieve stable regional total production estimates, let alone provide a credible explanation of the mechanisms behind yield variability (Guo et al., 2024).

Beyond estimation accuracy, traditional workflows rarely provide an explicit, interpretable driver chain for production change. Prediction-only models have difficulty answering the question of why total production and yield changed, which limits their value for risk assessment, scenario simulation, and management decisions (Islam et al., 2022). Attribution analysis often stays at post-hoc statistical association rather than a closed evidence loop (Islam et al., 2022). Yield variability is driven by a diverse and open set of factors, including meteorological anomalies (De Vos et al., 2025), phenological differences (Wang et al., 2023), soil moisture conditions (Yang et al., 2021), management practices (Mena et al., 2025), and other ecological constraints. Therefore, an attribution framework should construct an explicit evidence chain that can accommodate this open set of drivers, rather than tying explanations to any single data stream. In this context, large language models (LLMs) provide a promising pathway for transforming heterogeneous evidence into coherent mechanism explanations (Li et al., 2025). Nevertheless, directly applying general multimodal LLMs to agricultural problems often leads to hallucinations, largely due to insufficient vision-language alignment and limited perception of domain-specific physical features (Wu et al., 2025). Hence, attribution requires a knowledge-driven and evidence-constrained reasoning strategy that injects immutable factual evidence and domain knowledge into the reasoning process, so that explanations are supported by available quantitative results and less prone to free-form fabrication.

Under current technical trends, this study does not focus on incremental tweaks to existing workflows. Instead, it attempts to break the traditional yield-estimation pipeline by reconstructing the workflow from perception to estimation and then to attribution within a unified framework, so that it can both reduce uncertainty caused by multi-stage error propagation and provide structured evidence for later mechanism explanations. Therefore, this study aims to develop an intelligent agricultural framework that integrates environmental perception, total production and yield estimation, and mechanism attribution into a closed loop. To address these issues, this study proposes and develops a knowledge-driven holistic perception and attribution framework for intelligent agricultural modelling, named the Single-source Holistic Perception and Attribution Large Language Model (SHiPA-LLM).

The expected overall effect of this framework is to achieve robust estimation of key regional yield elements based on a single and transferable unified representation, and to generate auditable driver-attribution explanations under knowledge and evidence constraints, thereby supporting risk assessment and scenario simulation under uncertainty. To support this overall goal, we further define three sub-objectives. First, we construct a unified perception entry based on embedding representations from geo-foundation models (GFMs), to reduce dependence on multi-source heterogeneous inputs. As shown by Brown et al. (2025), pretrained models such as AlphaEarth can encode spectral information and environmental semantics into unified embeddings, enabling downstream tasks to obtain holistic habitat representations without explicitly relying on multi-source inputs and reducing dependence on multi-source alignment. Second, at the estimation level, we explicitly organize the structural elements related to total production and introduce necessary constraints, so that relationships among key variables better match the basic structure of yield formation, and thus reduce the error accumulation and unstable propagation found in traditional step-by-step workflow. Third, at the attribution level, we introduce a knowledge-driven, evidence-constrained reasoning mechanism. It takes quantitative estimation results and available environmental/process evidence as joint inputs, to reduce hallucination risk and improve the consistency and verifiability of explanations. To validate the proposed SHiPA-LLM framework, we select soybean as the representative scenario in this study, given its strategic importance and high sensitivity to climate disturbances. However, it should be emphasized that the perception/estimation backbone is crop-agnostic by design, as the geo-foundation model is pretrained across diverse tasks and crop types, and the attribution knowledge base can be swapped or adapted to transfer the framework to different crops and regions.

2 Study Area and Data

2.1 Study Area

This study focuses on Northeast China (NEC) as the study area, covering Heilongjiang, Jilin, Liaoning, and eastern Inner Mongolia (Figure 1(a)(b)). Northeast China is one of the most important agricultural production regions in the world, contributing more than 60% of China's total soybean production and playing a key role in the national food supply.

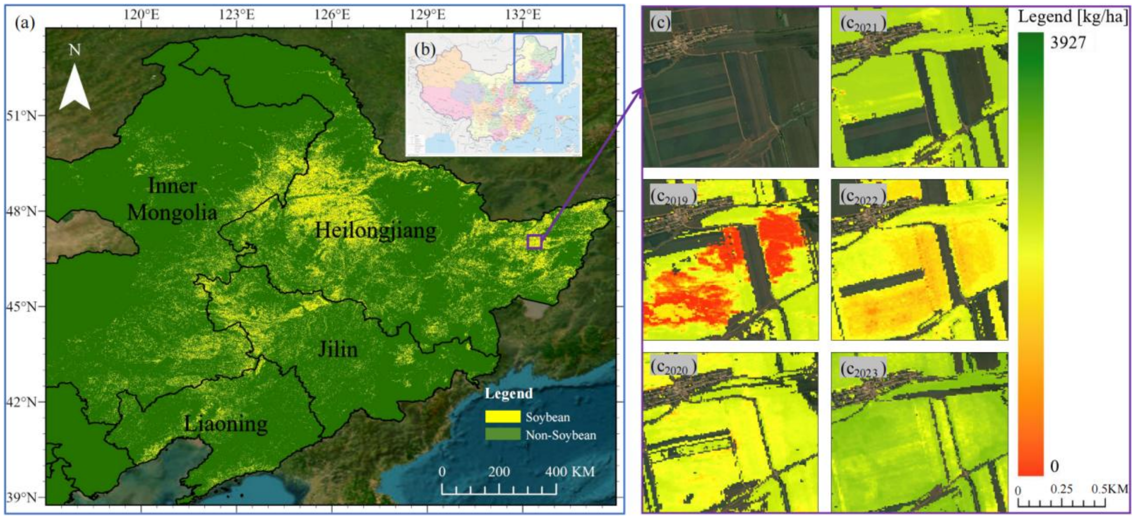

Figure 1: Study region and example yield maps. (a) Soybean harvested area footprint aggregated over five years (pixels harvested at least once are labelled as soybean). (b) Location of the study region in China. (c) A representative image patch (1.28 km × 1.28 km); the purple box of (a) indicates the location of the example in (c) (not its spatial extent; see scale bar). (c2019–c2023) Corresponding yield (kg/ha) examples for the patch from 2019 to 2023.

Agricultural production in NEC is large-scale and highly mechanized, with extensive contiguous farmland. Crops are mainly planted in monoculture or rotation systems. This relatively homogeneous planting pattern reduces interference from mixed pixels, but it also places higher requirements on the spatial coverage and computational timeliness of the monitoring system. NEC has a temperate monsoon climate, with a short growing season and limited heat resources. In recent years, extreme events such as spring drought, summer flooding, and low-temperature cold stress have become more frequent, leading to strong inter-annual variability in yield. In addition, state-owned farms and small, scattered operations coexist in the region. Management differences in irrigation and fertilization can still cause clear yield differences under similar climate conditions, providing a representative context for analysing how environmental factors and production factors jointly affect yield.

2.2 AEF Embeddings Data

The main remote sensing input in this study comes from the AEF (AlphaEarth Foundations) model released by Google DeepMind (Brown et al., 2025). AEF is a geo-foundation model, pretrained on large-scale high-resolution satellite imagery (e.g., Sentinel-1 data, Sentinel-2 data, and others). Its goal is to compress complex land-surface information into stable and transferable representations.

In practical use, this study directly uses the annual-scale 64-dimensional embedding vectors generated by AEF as the unified input. Through self-supervised learning on multi-source data, the embeddings integrate land-surface observation semantics that are closely related to this study into a compact latent space, including surface textures, vegetation growth processes, and phenological dynamics. Therefore, compared with traditional multispectral features, they have stronger noise robustness and better semantic consistency.

To ensure consistency between input scale and supervision scale, the AEF embeddings used in this study match the gridded aggregation used for the yield reference estimates in spatial coverage: each sample corresponds to an area of about $1.28\,\text{km}\times1.28\,\text{km}$, which is also consistent with the spatial footprint of one AEF embedding tile.

2.3 Yield Data

To obtain a reliable regional-scale soybean yield reference, this study uses the NortheastChinaSoybeanYield20m dataset (Xu et al., 2026) as the yield reference estimates (Figure 1(a)(c)(c2019-c2023)). This dataset provides pixel-level yield information for soybean in Northeast China from 2019 to 2023, with a spatial resolution of 20 m, and it can characterize spatial and inter-annual variations of soybean yield in NEC.

The accuracy of the dataset was evaluated by in-situ measured and statistical data. The overall accuracy was 287.44 kg/ha and 272.36 kg/ha in the root mean squared error (RMSE) for field and regional scale, respectively. Stable results were achieved through the years with mean relative error (MRE) on average of 11.46 % in municipal scale and 7.94 % in provincial scale.

2.4 Environmental Factors

To build the environmental factor reference data required in this study, we use the ECMWF/ERA5_LAND/MONTHLY_AGGR dataset provided by the Google Earth Engine (GEE) platform as the data source. This dataset is a monthly aggregated product derived from hourly ERA5-Land reanalysis data, and it provides globally consistent land-surface environmental variables with 150 factors as environmental factors reference observed dataset (Sabater, 2019).

ERA5-Land reanalysis has a spatial resolution of about 0.1° in a gridded format. The monthly aggregated product on GEE inherits its global coverage and relatively high-resolution characterization of land-surface environments, which makes it convenient to extract continuous environmental factor sequences and reproduce them at the regional scale. Therefore, this dataset can provide monthly mean descriptions for state-type environmental conditions such as temperature, radiation, and soil moisture, and it can also provide monthly total descriptions for accumulated-type hydro-thermal processes such as precipitation and evapotranspiration. This makes it suitable for organizing and summarizing environmental states during the crop growing season.

2.5 Knowledge Base Literature Sources

To ensure the accuracy and scientific rigour of yield-attribution explanations, this study constructs a high-confidence agricultural knowledge base to explain the environmental and physiological driving mechanisms of soybean production. The knowledge base strictly follows literature screening standards. We use Google Scholar (https://scholar.google.com/) as the search engine, with the keyword “factors affecting soybean yield”. We only include review papers and highly cited meta-analyses published in journals ranked JCR Q2 and above. Finally, we counted the citations of each paper as of 2026-02-20, and selected the 100 most-cited papers as the literature sources of the knowledge base.

During the attribution stage, this knowledge base serves as authoritative external evidence to support explanations of yield variability. By anchoring attribution analysis in peer-reviewed consensus knowledge, we ensure that all explanations of driving factors come from established agronomic research, rather than relying only on internal correlations of the model, thereby improving the scientific credibility and practical value of the conclusions.

3 Methodology

3.1 Overview of the Single-source Holistic Perception and Attribution Large Language Model (SHiPA-LLM)

This study develops SHiPA-LLM that couples geospatial perception with attribution-oriented reasoning (Figure 2). The model takes AEF embedding features as the only remote sensing input and produces a patch-level representation of soybean production states and environmental conditions in a unified forward pass. Specifically, it estimates total production and harvested area, derives yield per unit area through a deterministic physical constraint, and simultaneously reconstructs growing-season meteorological variables. These numerical outputs are subsequently integrated into a knowledge-base-augmented LLM module to generate vision-grounded attribution narratives, ensuring that interpretation is anchored to physically meaningful evidence rather than free-form speculation.

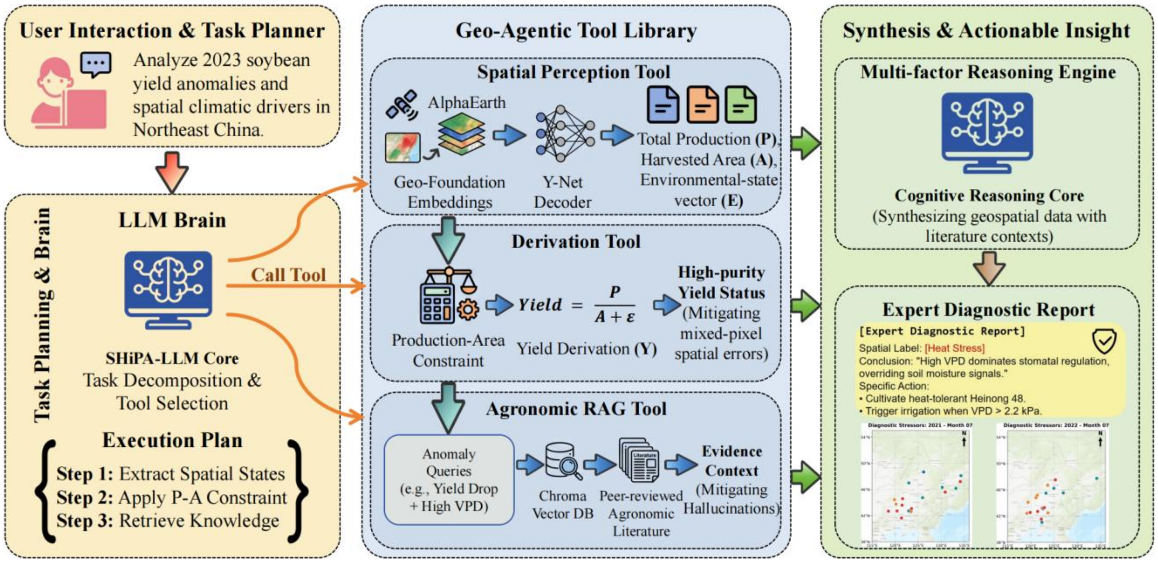

Figure 2: The overview of the Single-source Holistic Perception and Attribution Large Language Model (SHiPA-LLM).

A key design choice is motivated by the compressed nature of embedding representations. Although AEF embeddings encode land-surface texture, vegetation dynamics, and habitat semantics in a compact latent space, they do not explicitly preserve all radiometric details required for stable direct regression of ratio-type agronomic variables. Yield per unit area is inherently a quotient of total production and harvested area; modelling it as a direct target often amplifies minor inconsistencies in the underlying latent representation. To enforce physical plausibility and improve robustness, the proposed framework adopts a production-and-area-first strategy: total production and harvested area are predicted explicitly, and yield is obtained through an immutable physical layer. In parallel, the reconstruction of meteorological variables provides the environmental evidence needed for mechanism-oriented attribution. The overall workflow therefore forms a closed loop from perception to structured explanation, enabling interpretable regional soybean production estimation and driver analysis. The implementation of this methodology is organized into three parts: the quantitative estimation network (Y-Net), the data validation strategy, and the LLM-based attribution reasoning mechanism.

3.2 Spatial Perception Tool and Derivation Tool

Figure 3 illustrates the architecture of the proposed Physics-Aware Dual-Branch Y-Net. As the quantitative estimation backbone of the SHiPA-LLM framework, this network is responsible for mapping single-source AEF embeddings into structured production and environmental evidence. The workflow operates in a unified forward pass where the input embeddings are first encoded by a shared convolutional backbone to extract latent features. These features are then decoupled into two task-specific branches to simultaneously predict production states (total production and harvested area) and reconstruct meteorological variables. This design ensures that the subsequent attribution analysis is grounded in physically consistent and numerically robust estimations.

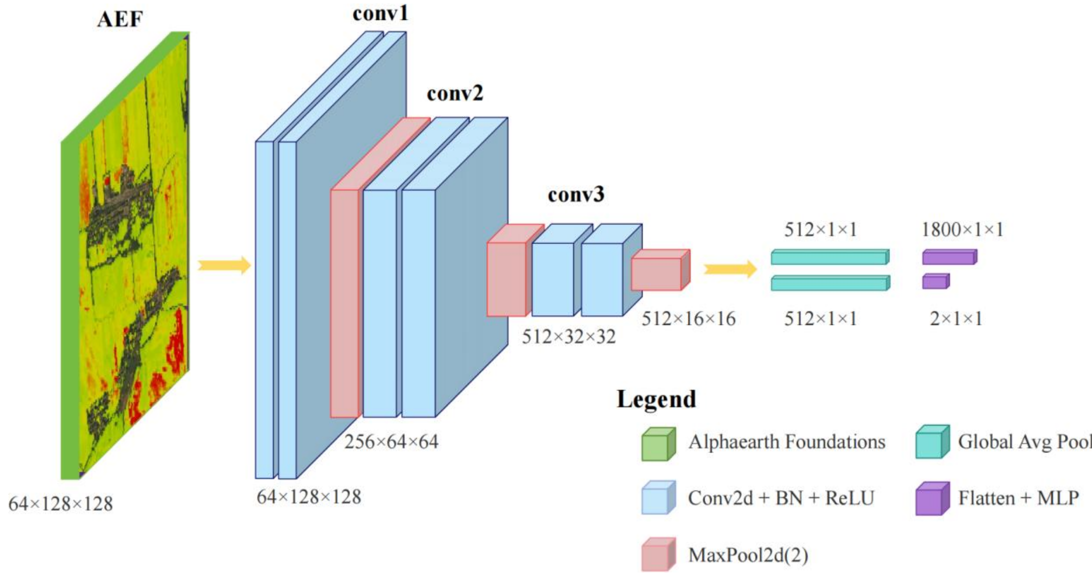

Figure 3: Overview of Dual-Branch Y-Net design.

3.2.1 Input Representation and Geometric Alignment

The deep learning component operates on AEF embedding rasters with 64 channels. To guarantee geometric consistency of convolutional receptive fields across latitudes, each sample is processed under a dynamic UTM projection. For a given patch centre, the UTM zone is determined from longitude, the embedding image is reprojected accordingly, and a square patch is extracted by centre cropping. The resulting model input is expressed as

$$\boldsymbol{X}_i \in \mathbb{R}^{64\times128\times128}, \tag{1}$$

where $\boldsymbol{X}_i$ denotes the AEF embedding tensor of the i-th sample, 64 is the embedding channel dimension, 128×128 is the spatial size of the cropped patch in pixels, and $\mathbb{R}$ denotes the real-valued domain.

3.2.2 Supervision Signal Construction and Sampling Strategy

Supervision is defined by production states and environmental states. The production reference dataset is the 20 m gridded product NortheastChinaSoybeanYield20m. For each patch, we aggregate valid soybean pixels to obtain patch-level total production P_i (kg) and harvested area A_i (ha). The yield Y_i (kg/ha) is then computed as $Y_i{=}P_i/A_i$, which serves as the reference variable for constraint-based learning and evaluation. We further define a 3-dimensional production-state vector:

$$(P_i,A_i,Y_i) \in \mathbb{R}^3. \tag{2}$$

Environmental reference variables are derived from the ERA5-Land reanalysis and cover all months within one year. For each patch, we construct an environmental-state vector by concatenating monthly statistics and derived indicators:

$$E_i \in \mathbb{R}^{1800}, \tag{3}$$

where E_i denotes the environmental state of the i-th sample, consisting of 150 environmental factors per month × 12 months.

To mitigate the long-tailed distribution commonly observed in agricultural production, we apply stratified sampling based on yield. Specifically, we first split all samples into a training set and a validation set with an 8 : 2 ratio, and then construct the training set by yield-stratified sampling with 5000 samples. We adopt a 10-bin uniform sampling strategy to preserve representation across different production regimes, which improves sensitivity to extreme low- and high-production cases and reduces mean-collapse behaviour during optimization.

3.2.3 Network Architecture and Feature Extraction

The proposed network follows a Physics-Aware Dual-Branch Y-Net design with a shared convolutional backbone and two task-specific heads. Given the input $\boldsymbol{X}_i$, the backbone extracts a high-dimensional feature map:

$$\boldsymbol{F}_i = f_\theta(\boldsymbol{X}_i), \quad \boldsymbol{F}_i \in \mathbb{R}^{512\times16\times16}, \tag{4}$$

where $\boldsymbol{F}_i$ is the latent feature representation of the i-th sample, $f_\theta(\cdot)$ denotes the backbone parametrized by θ, 512 is the number of feature channels, and 16×16 is the spatial resolution after downsampling.

The production branch regresses total production and harvested area as:

$$(\widehat{P}_i, \widehat{A}_i) = g_\phi(\boldsymbol{F}_i), \tag{5}$$

where $\widehat{P}_i$ and $\widehat{A}_i$ are the predicted total production and harvested area of the i-th patch, and $g_\phi(\cdot)$ denotes the regression head with parameters ϕ.

In parallel, the environment branch reconstructs the 1800-dimensional meteorological state:

$$\widehat{E}_i = \mathrm{h}_\psi(\boldsymbol{F}_i) \tag{6}$$

where $\widehat{E}_i$ denotes the predicted meteorological vector and $\mathrm{h}_\psi(\cdot)$ is the environmental regression head parametrized by ψ. This auxiliary reconstruction task encourages the shared representation to preserve physically relevant environmental semantics, which later serve as grounded evidence for attribution.

3.2.4 Physical Consistency Constraints and Loss Functions

Instead of regressing yield directly, the model derives yield per unit area via an immutable physical layer:

$$\widehat{Y}_i = \frac{\widehat{P}_i}{\widehat{A}_i + \epsilon}, \tag{7}$$

where $\widehat{Y}_i$ is the derived yield, ϵ is a small constant to avoid division by zero, and $\widehat{P}_i$ and $\widehat{A}_i$ follow Eq. (5). Since learning is conducted under Z-score normalization for numerical stability, the division in Eq. (7) is performed in the original physical space after inverse normalization of $\widehat{P}_i$ and $\widehat{A}_i$, ensuring that ratio computation remains physically meaningful.

The task-level errors are defined through mean squared error (MSE):

$$\mathscr{L}_P=\mathrm{MSE}(\widehat{P},P),\quad \mathscr{L}_A=\mathrm{MSE}(\widehat{A},A),\quad \mathscr{L}_Y=\mathrm{MSE}(\widehat{Y},Y),\quad \mathscr{L}_E=\mathrm{MSE}(\widehat{E},E), \tag{8}$$

where $\mathscr{L}_P$, $\mathscr{L}_A$, $\mathscr{L}_Y$, and $\mathscr{L}_E$ correspond to errors of total production, harvested area, physics-derived yield, and meteorological reconstruction, respectively; $\widehat{P}$, P, $\widehat{A}$, A, $\widehat{Y}$, Y, $\widehat{E}$, E denote predictions and reference estimates over a minibatch or the dataset; and MSE($\cdot$) computes the squared error averaged over samples (and over dimensions for vector targets).

To reduce computational overhead and avoid over-parametrized weighting, all 1800 environmental factors are supervised under a single coefficient, because they originate from the same reanalysis source and are decoded from the same embedding-based visual evidence. The production-related objectives, however, are balanced through adaptive task weighting based on homoscedastic uncertainty (Kendall et al., 2018). The final joint objective is:

$$\mathscr{L}=\frac{1}{2\sigma_P^2}\mathscr{L}_P+\log\sigma_P+\frac{1}{2\sigma_A^2}\mathscr{L}_A+\log\sigma_A+\frac{1}{2\sigma_Y^2}\mathscr{L}_Y+\log\sigma_Y+\frac{1}{2\sigma_E^2}\mathscr{L}_E+\log\sigma_E, \tag{9}$$

where $\mathscr{L}$ denotes the overall training objective; $\mathscr{L}_P$, $\mathscr{L}_A$, $\mathscr{L}_Y$, and $\mathscr{L}_E$ are the MSE losses for total production, harvested area, physics-derived yield, and climate reconstruction, respectively; σ_P, σ_A, σ_Y, and σ_E are learnable homoscedastic uncertainty parameters that adaptively balance the four objectives during optimization. Notably, the climate term is constructed by aggregating all 1800 environmental factors into a single reconstruction loss $\mathscr{L}_E$, i.e., factor-wise reweighing is not performed, and the entire meteorological vector is supervised under a shared task-level weight σ_E.

3.3 Agronomic RAG Tool

To support mechanism attribution and evidence retrieval for low-yield anomalies, we develop an integrated workflow that combines a literature embedding-based vector knowledge base with case-adaptive retrieval and evidence-constrained generation. The workflow takes as inputs the Y-Net outputs for each case, including total production, yield, and harvested area, as well as the results of 1,800 environmental factors across 12 months in the year. It also uses high-quality domain papers and the environmental-factor regression accuracy during Y-Net training as external knowledge sources to retrieve relevant evidence for each case. The workflow can automatically determine the yield condition. By retrieving literature and jointly considering environmental-factor regression accuracy, it automatically selects the environmental factors that are most critical (such as growing months in 12 months) for yield attribution for analysis. Finally, under a fixed template, it generates a traceable three-part report (Overview-Attribution-Recommendations) (Arslan et al., 2024).

3.3.1 Document parsing and vector knowledge base construction

We first parse domain-relevant high-quality PDF papers into page-level text units, denoted as

$$D=\{d_i\}_{i=1}^{N}, \tag{10}$$

where D is the set of page-level text units; d_i is the i-th unit; and N is the total number of parsed units. Parsing failures or empty texts are removed to ensure corpus validity and robustness.

Each page-level unit is then decomposed into a set of overlapping semantic chunks via recursive text splitting:

$$S=\{s_j\}_{j=1}^{M}, \quad |s_j|\leq L, \quad \text{overlap}=O, \tag{11}$$

where S is the chunk set; s_j is the j-th chunk; M is the total number of chunks; $|s_j|$ denotes the chunk length (in characters); L is the maximum chunk length; and O is the overlap length between adjacent chunks. In this study, we set L=1000 characters and O=200 characters to reduce boundary information loss and improve cross-chunk recall.

For each chunk s_j, we compute its embedding using a pre-trained sentence encoder:

$$e_j=f_\theta(s_j)\in\mathbb{R}^{dim}, \tag{12}$$

where $f_\theta(\cdot)$ is a sentence embedding model (Sentence-Transformers: all-MiniLM-L6-v2); e_j is the embedding of chunk s_j; and dim is the embedding dimension. We then store the triples $\{(s_j,e_j,meta_j)\}_{j=1}^{M}$ in a Chroma vector database for persistent indexing, where $meta_j$ records provenance information (e.g., source file and page number) for traceability. For experimental controllability and reproducibility, the database is cleared and rebuilt at each run to ensure consistency with the current document collection.

3.3.2 Case-adaptive Retrieval and Evidence Context Construction

During retrieval and analysis, for each low-yield case c (including the predicted yield and multi-variable monitoring sequences), we first generate a mechanism-oriented adaptive query (DeepSeek-V4):

$$q=G(c), \tag{13}$$

where c denotes one low-yield case; $G(\cdot)$ is a lightweight generative model used for query formulation; and q is the resulting retrieval query. This design helps avoid overly localized keywords that may bias evidence selection.

We embed the query using the same sentence encoder:

$$e_q=f_\theta(q), \tag{14}$$

where e_q is the embedding vector of query q.

We then perform nearest-neighbor search in the vector database using cosine similarity and return top-k (in this study, we set $k = 50$) chunks:

$$\text{sim}(q,s_j)=\cos(e_q,e_j)=\frac{e_q^{\top} e_j}{\|e_q\|_2\|e_j\|_2}, \qquad R_k(q)=\text{TopK}_{s_j\in S}\,\text{sim}(q,s_j), \tag{15}$$

where $\text{sim}(q,s_j)$ is the similarity between query q and chunk s_j; $\cos(\cdot)$ is cosine similarity; $\|\cdot\|_2$ is the ℓ_2 norm; $R_k(q)$ is the set of retrieved top-k chunks; and k is the number of returned chunks.

Since multiple high-similarity chunks may originate from the same paper, we deduplicate retrieval results by source document and construct an evidence context:

$$C(c)=\text{Concat}\left(U\ (R_k(q))\right), \tag{16}$$

where $U(\cdot)$ denotes deduplication by source document (retaining representative chunks per paper); Concat(·) concatenates selected chunks into a single context; and $C(c)$ is the evidence context for case c.

3.3.3 Evidence-constrained Prompting and Three-part Report Generation

Finally, we combine case information and evidence context to build a strongly constrained prompt:

$$Prompt(c)=\Phi\left(c,C(c)\right), \tag{17}$$

where $Prompt(c)$ is the final prompt fed to the report generator; and $\Phi(\cdot)$ is a fixed-structure template function that organizes the case information and evidence context into a standardized input.

Under this template, the generator (DeepSeek-V4) produces a three-part report (Overview-Attribution-Recommendations). The overview section summarizes the production status and anomalies of the case (table 1). The attribution section needs to jointly consider the regression accuracy of environmental factors, extract key abnormal signals from the case data, and cite evidence snippets with clear indices (source and page numbers) to ensure traceability. The recommendation section then provides management suggestions or risk warnings based on the attribution mechanisms. This design enables traceable outputs by combining data-driven anomaly identification with literature-based mechanistic evidence, and it is tailored to the soybean production scenario in Northeast China.

Stressor label	Required evidence direction	Main interpretation
Heat stress	High temperature-related factor	Thermal stress screening
Drought	Moisture deficit or low precipitation	Water deficit screening
Waterlogging	Excess precipitation or soil moisture	Excess-water screening
Cold stress	Low temperature-related factor	Low-temperature screening
Normal condition	No supported stressor direction	No dominant stressor detected

Table 1: Directional evidence rules used to constrain monthly stressor labels.

3.4 Evaluation Strategy and Robustness Analysis

To comprehensively validate the performance and reliability of the quantitative estimation backbone within the SHiPA-LLM framework, this section establishes a multi-dimensional evaluation strategy. The assessment begins by benchmarking the proposed network against representative baseline methods to demonstrate its predictive efficacy and computational efficiency. Beyond basic accuracy, we further investigate the model's structural stability and generalization boundaries under complex practical constraints. This includes evaluating the network's resilience to incomplete supervision signals, analysing the numerical stability of physics-derived yield across different fragmented area conditions, and rigorously testing its temporal generalization ability against inter-annual climate variability.

3.4.1 Baseline Settings

The main focus of this work is to build a modelling workflow for regional production monitoring. Based on this positioning, the baseline comparison follows a non-inferiority mindset rather than a strict State-of-the-Art (SOTA) validation. Under the same inputs and evaluation settings, if the proposed model achieves performance at the same order of magnitude as mainstream methods on the main-task metrics, it is sufficient to show that this workflow remains predictive-effective while being feasible to further extend with constraint and explanation modules. Meanwhile, because large-scale operation is required, runtime is also one of our key metrics. Although complex models may have a slight advantage in accuracy, their long runtime makes them unsuitable for our workflow of large-scale operational production monitoring.

The baseline methods cover two representative groups. The first group includes common traditional regression methods such as XGBoost (Chen, 2016), which serve as performance baselines under relatively low modelling complexity. The second group includes mainstream deep network backbones (ResNet-152 (He et al., 2016), ConvNeXtV2 (Woo et al., 2023), RepViT (Wang et al., 2024)), which are used to evaluate the upper bound of performance and the computational cost under the same inputs, across different network capacities and architectural choices. All methods report R^2 and RMSE for total production and harvested area on the same test set, and we also record training and inference time to characterize the trade-off between accuracy and computational cost. For a fair comparison of runtime, we run all code under the same configuration: CPU: 25 vCPU Intel(R) Xeon(R) Platinum 8470Q; GPU: RTX 5090 (32GB) ×1; Memory: 90GB.

3.4.2 Ablation Study

This ablation experiment is used to evaluate the train ability and degraded-operation ability of the proposed framework when supervision signals are incomplete. In real applications, regional-scale agricultural statistics often suffer from incomplete labels, for example, only total production is available but harvested area is missing, or climate-related supervision and the evidence layer cannot be introduced due to data availability and consistency issues. To test the model sensitivity to missing supervision, we construct three training configurations: Production-only uses only total production supervision; Production + Area (w/o climate) uses joint supervision of total production and harvested area but does not enable climate-related components; and *Proposed* is the full model. The focus of this comparison is not to pursue the best accuracy for a single configuration, but to examine whether the main tasks remain at the same order of magnitude under different supervision availability conditions, and thus to verify the modularity and deployment flexibility of the framework.

3.4.3 Yield Derivation Strategy and Thresholds

This section evaluates the applicability and failure modes of two implementation paths for yield estimation under different sample conditions. Since yield is a ratio-type variable, when harvested area is small or the relative estimation error is large, yield can suffer from a numerical amplification effect and become unstable. Therefore, we compare three strategies: "Direct Yield", which directly regresses yield with the network;"Non-constraints Yield", which directly computes yield by directly dividing predicted total production by predicted harvested area (without physical-consistency constraints); "Physics-derived Yield", which computes yield as a ratio in real space using the predicted total production and harvested area, so as to maintain consistency with production and area.

To explicitly test the impact of small-area samples on yield stability, we apply harvested area proportion thresholds for filtering, and only keep samples whose harvested area accounts for no less than the given proportion P_p of the total patch area (thresholds from 50% to 90% in the table). Under each threshold, we compute R^2 and RMSE for yield. For cases where $R^2<0$, to improve readability we mark them as NaF in the table note, meaning that under this setting the model's explanatory power on the threshold subset is worse than a constant baseline, and thus the results fall into an unusable or unstable regime.

3.4.4 Temporal Generalization Analysis

To evaluate the robustness of the proposed SHiPA-LLM estimation backbone under inter-annual climate variability and changes in planting patterns, this study adopts a stricter Leave-One-Year-Out (LOYO) cross-validation strategy. Specifically, within the 5-year dataset, we alternately select one year as an independent test set and use the remaining four years as the training set. This setting simulates a real operational forecasting scenario, where knowledge from historical years is used to infer performance in an unknown future year.

3.4.5 Evaluation Metrics for Agronomic RAG Tool

$$S_i=\{\widehat{P}_i,\widehat{A}_i,\widehat{Y}_i,\widehat{E}_i\}. \tag{18}$$

For climate-related claims, we enforce directional consistency: statements such as anomalously low precipitation or high temperature stress must match the sign of the corresponding anomalies in $\widehat{E}_i$ under a predefined anomaly criterion (e.g., negative/positive deviation in the standardized climate factors). In addition, each mechanism statement is required to cite retrieved evidence passages, and we record whether the cited passages explicitly mention the same stressor-response relationship. These rule-based checks ensure that the attribution module complements quantitative prediction with auditable, evidence-grounded interpretations rather than free-form narratives.

4 Results

4.1 Sampling Profile and Target Characteristics

Before evaluating the model's predictive performance, it is essential to understand the statistical and spatial characteristics of the underlying data distributions. Regional agricultural data inherently exhibits a long-tailed distribution, where the majority of parcels fall within an average yield range, while extreme low or high yield cases are relatively sparse. To ensure that the model learns robust representations across all production levels without collapsing to the mean, we employed a stratified sampling strategy for the training set, while keeping the test set aligned with the natural distribution of the region. As illustrated in figure 4, clarifying this divergence between the balanced training profile and the natural testing environment provides necessary context for interpreting the subsequent accuracy metrics and generalization tests.

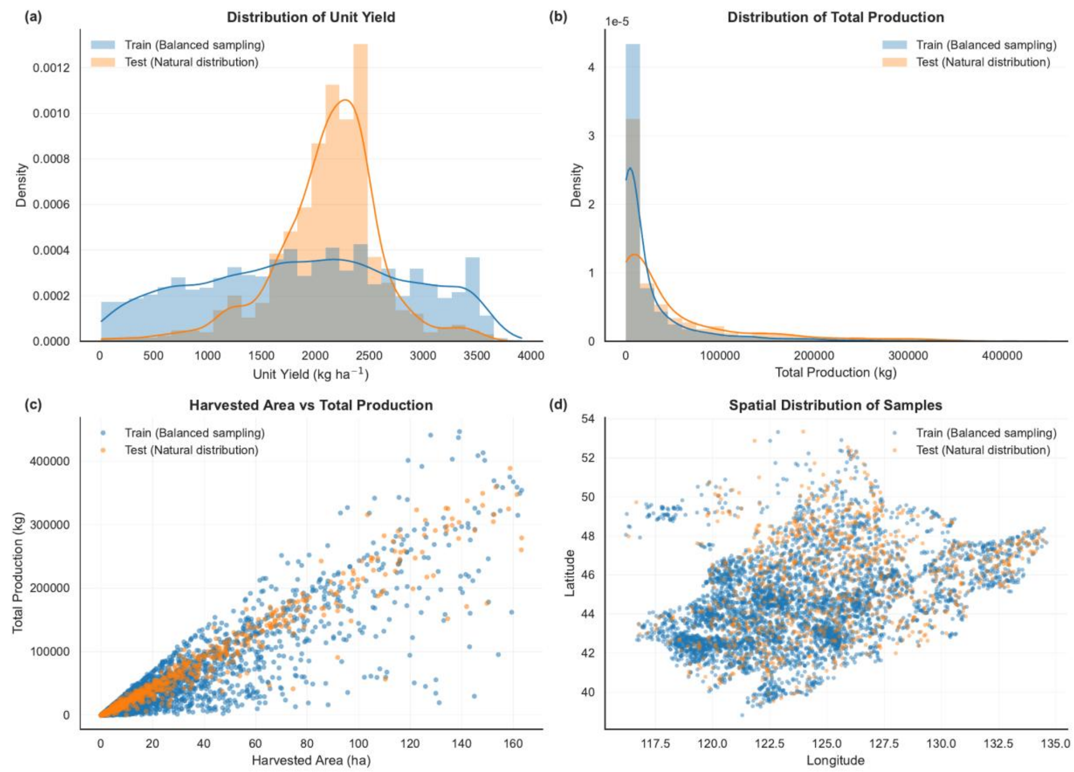

Figure 4: Comparison between the training set (balanced sampling) and the test set (natural distribution). (a) Distribution of yield. (b) Distribution of total production. (c) Scatter plot of harvested area versus total production. (d) Spatial distribution of samples in the study region.

As shown in figure 4(a), the distribution shapes of yield differ between the training set and the test set. The training set covers a wider yield range and shows a flatter density curve, while the test set is more concentrated, with a clearer peak in the range of about 1700–2500 kg/ha. Figure 4(b) shows that yield has a clear right-skewed distribution. Both datasets are dominated by low-total-yield samples and have a long tail extending to high values. At the same time, the training set has a relatively higher sample density in the medium-to-high total-yield range.

Figure 4(c) presents the scatter relationship between harvested area and total production. It can be observed that total production generally increases with harvested area, and sample points are denser in the small-area range. As area increases, the scatter range becomes wider, indicating that total production can vary substantially under similar harvested area conditions. Figure 4(d) shows the spatial distribution of samples. The training set and test set have consistent coverage over the study region and similar spatial patterns, which meets the standard of spatially random sampling. Training samples are denser, while test samples are relatively sparser, which matches the difference in sampling size between the two sets.

4.2 Accuracy of Spatial Perception Tool and Derivation Tool

4.2.1 Total Production and Harvested Area

The evaluation results on the independent test set show that SHiPA-LLM can effectively interpret soybean production states from AEF embedding features. Figure 5 presents the scatter distributions between the predicted values and the ground-truth values for total production and harvested area. For total production estimation, the model achieved a result of R^2=0.7287, with an RMSE of 43,049.7 kg. The scatter points are overall closely distributed around the 1:1 line, indicating that the model maintains good consistency across different production levels, without an obvious systematic bias. Although the dispersion slightly increases in the high-production range (>300,000 kg), which is usually attributed to canopy saturation effects in high-density planting areas, the model still successfully captures the overall regional production gradient. The estimation accuracy for harvested area is slightly better than that for total production (Figure 5), with R^2=0.7482 and RMSE controlled within 19.34 ha.

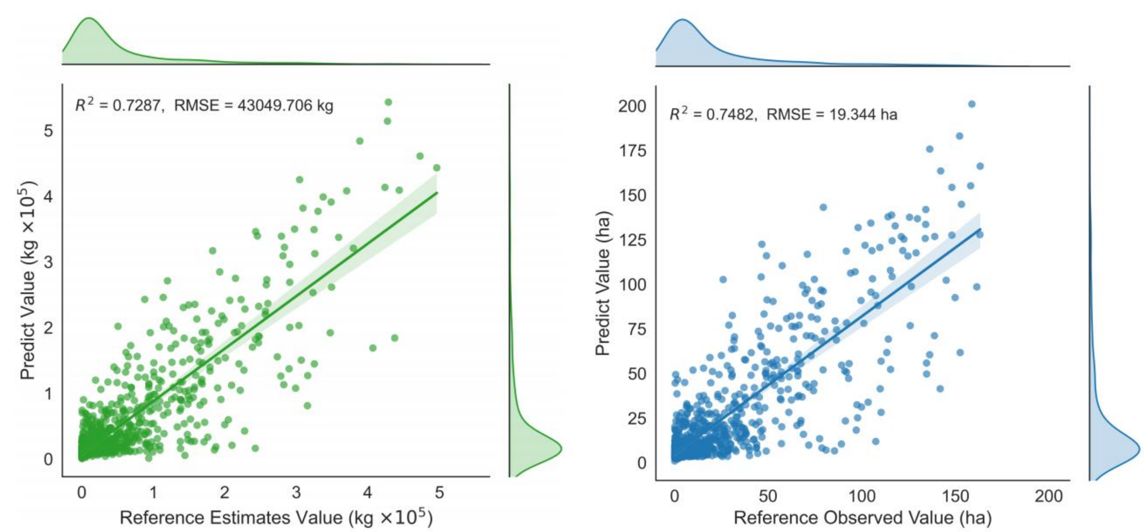

(a) Total Production (b) Harvested Area

Figure 5: Scatter plots comparing predicted values against reference estimates on the test set. (a) Total Production (kg) per patch. (b) Harvested Area (ha) per patch. The dashed line represents the 1:1 identity line.

To explore the adaptability boundary of the model across different agro-ecological zones, we spatially aggregated the test samples into 0.5° ×0.5° grids and mapped the spatial distributions of R^2 and RMSE (Figure 6). The results reveal strong geographic non-stationarity in model performance and show a clear core-periphery pattern. Importantly, RMSE is relatively uniform across the study region, while R^2 is higher in high-value areas. This indicates that the error magnitude is similar across regions, but the ability to explain local variation (variance explained) differs substantially in space.

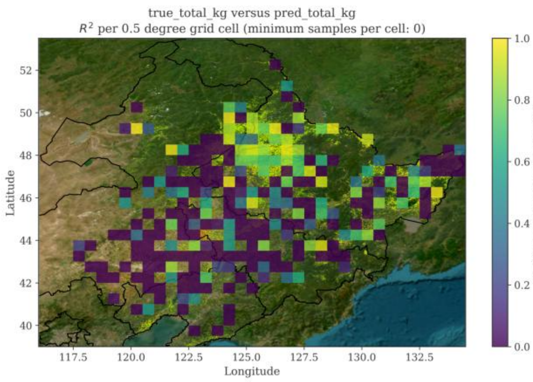

(a) R^2 of Total Production

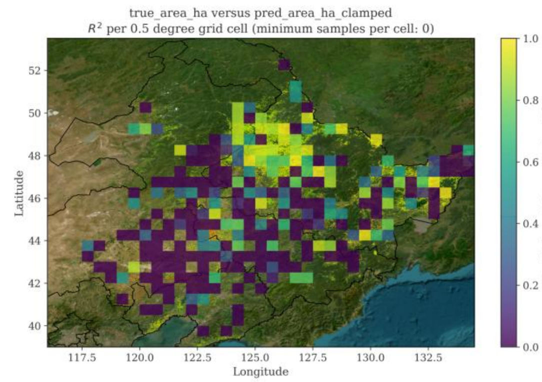

(b) R^2 of Harvested Area

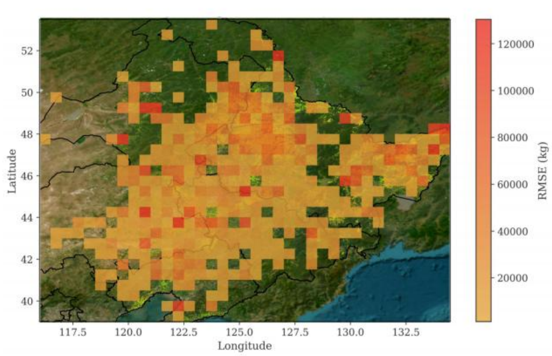

(c) RMSE of Production

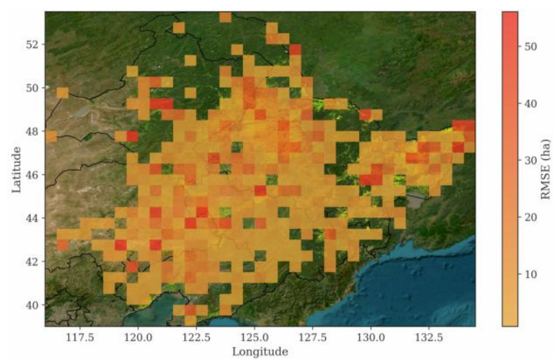

(d) RMSE of Harvested Area

Figure 6: Spatial distribution of the R^2 and RMSE aggregated on a grid.

From a broad geographic gradient, prediction accuracy does not show a systematic decline with increasing latitude or with changes in longitude. In both the northernmost Heihe area (latitude >50° N) and the southern Liaoning agricultural region, clusters with relatively high accuracy and relatively higher errors can be observed. This phenomenon strongly confirms that the model has good applicability across different latitudes and longitudes. In contrast to the weak association with geographic coordinates, the spatial performance of the model is more strongly coupled with production intensity, but this coupling mainly appears in R^2 rather than in RMSE. As shown in Figure 6 , RMSE does not form clear hotspot clusters in most areas, but instead shows a relatively uniform spatial texture. This suggests that the absolute error scale is broadly similar across ecological zones. However, Figure 6 shows that high-production/high-area (or more intensive) regions tend to have higher R^2 values. This means that in these regions, the model not only keeps a similar error level, but also better captures relative differences and the fluctuation structure among samples. In other words, higher R^2 in high-value regions is not because the error suddenly becomes smaller, but more likely because the ground-truth values in these regions have larger spatial/sample variance and stronger signals, so higher explained variance can be achieved under similar RMSE.

4.2.2 Environmental Factors Estimations

The full-sample regression tests show that the overall R^2 across the aggregated 150 factors is 0.6729, with a median of 0.7003. This statistical result demonstrates that AEF embedding vectors not only encode surface spectral features, but also capture meaningful associations between imagery and environmental factors.

Because the number of factors is large, we place the figures for most factors in the appendix A. Figure 7 presents the reconstruction performance for the two most decisive meteorological factors for soybean yield formation-temperature and precipitation. For 2 m air temperature (Figure 7(a)), the model achieves an almost perfect reconstruction accuracy, with R^2=0.9895,$RMSE$=1.373. Meanwhile, other heat-related factors, such as skin temperature (R^2=0.9889) and shallow soil temperature (Soil Temperature Level 1, R^2=0.9803,$RMSE$=0.0292), also rank among the top 10 factors with the highest prediction accuracy (see appendix A), which further supports the reliability of the model in sensing the thermal environment.

In contrast, reconstructing total precipitation is clearly more difficult, because precipitation processes have high randomness and discontinuity in their spatiotemporal distribution. Even so, the model still achieves a good performance for precipitation inference, with R^2=0.7879 (Figure 7(b)). This demonstrates that the model successfully learns the deep relationship between imagery and moisture conditions, and can thus infer the water environment experienced by fields based on AEF imagery.

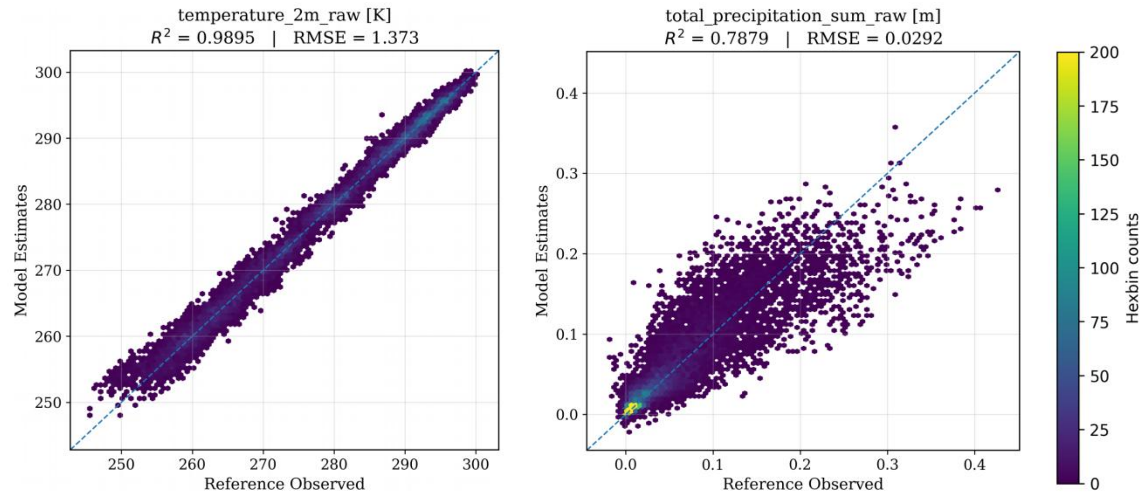

(a) Temperature (b) Precipitation (c)

Figure 7: Scatter plots of the predicted environmental factors variables versus observed environmental factors. (a) Temperature (K). (b) Precipitation (m). (c) Colorbar of Hexbin counts.

It should be noted that the reconstruction accuracy differs across meteorological factor categories due to objective physical differences. While the R^2 values for major agricultural factors such as temperature, radiation, and soil moisture are generally higher than 0.9, the prediction ability for some factors is relatively limited. The worst-performing factors mainly fall into two groups. The first group includes highly dynamic flux indicators, such as evaporation from vegetation transpiration ($R^2 \approx 0.007$). These variables are controlled by instantaneous weather conditions (e.g., wind speed and vapour pressure deficit), and their cumulative amounts are hard to capture using only annual static features. The second group includes sparsely distributed variables, such as lake mixed layer temperature and snow depth. Since most samples in the study area are cropland pixels, there are no lake water bodies or snow cover during the growing season, so the ground-truth labels contain many zeros or invalid values (data sparsity). This extreme imbalance in data distribution makes it difficult for the model to obtain sufficient gradient signals for effective learning. However, this limitation does not weaken the core value of the model in agricultural scenarios, because SHiPA-LLM shows reliable reconstruction accuracy for the key water, heat, and light factors that are most important for explaining soybean yield variability. This provides a solid data basis for the subsequent attribution analysis grounded in physical facts.

4.2.3 Yield Estimation Stability across Area Thresholds

From Table 2, clear differences emerge across harvested area thresholds. In the low-threshold regime (50%–70%), Direct yield regression remains numerically stable and consistently yields positive R^2 values (0.24–0.29), whereas the ratio-based strategies are unstable: Non-constraints Yield is reported as NaF for all three thresholds, and Proposed is NaF at 50%–60% and only reaches R^2=0.09 at 70%. This pattern suggests that when small harvested area samples are retained, yield estimation becomes highly sensitive to denominator noise. Simply dividing predicted production by predicted area without any constraint is particularly fragile, while the physically consistent design alleviates but does not fully eliminate the instability under small-area conditions. In terms of practical usability, Direct Yield regression is relatively preferable in this regime; however, its R^2 remains low, indicating limited explanatory power for yield and restricted reliability for downstream use.

Threshold	Direct Yield		Non-constraints Yield		Proposed	
	R^2	RMSE (kg/ha)	R^2	RMSE (kg/ha)	R^2	RMSE (kg/ha)
50%	0.24	376.4	NaF	NaF	NaF	373.4
60%	0.29	350.1	NaF	NaF	NaF	366.9
70%	0.28	310.4	NaF	NaF	0.09	347.9
80%	0.15	311.6	0.02	386.85	0.32	291.9
90%	0.25	247.6	0.24	332.26	0.63	233.0

Table 2: Yield performance under different harvested area proportion thresholds (keeping samples with harvested area proportion $\geq P_p$). "Direct Yield" means directly regresses yield; "Non-constraints Yield" means to computes yield by directly dividing predicted total production by predicted harvested area (without physical-consistency constraints); "Proposed" means derives yield under the physical-consistency design. NaF indicates unstable cases where $R^2<0$ or $RMSE>1000$ (reported as NaF for readability).

As the threshold increases, the advantage of the physically consistent derivation becomes much more evident. At 80%, Proposed improves to R^2=0.32 with RMSE =291.9 kg/ha, outperforming Direct Yield (R^2=0.15, RMSE =311.6 kg/ha) and Non-constraints Yield (R^2=0.02, RMSE =386.85 kg/ha). At 90%, Proposed further increases to R^2=0.63 with RMSE =233.0 kg/ha, whereas Direct Yield remains in the range of 0.15–0.25 and Non-constraints Yield stays noticeably weaker (R^2=0.24, RMSE =332.26 kg/ha). Importantly, the gap between Non-constraints Yield and Proposed at high thresholds isolates the contribution of the physical-consistency design: the performance gain is not solely due to taking a ratio, but to enforcing a coherent production-area relationship that reduces error amplification in yield. Overall, these results support a threshold-dependent use strategy: Direct Yield regression provides a stable fallback when small-area samples cannot be filtered, while the physically consistent derivation becomes the preferred option after excluding small-area cases and reaches a practically usable level at the 90% threshold.

4.3 Performance Comparison and Robustness Assessment

4.3.1 Accuracy Comparison against Baseline Models

Table 3 summarizes the test-set performance of different methods. The overall trend is clear: traditional machine learning methods lag behind deep models on both tasks. This suggests that when using only annual embedding representations as inputs, shallow regressors cannot fully capture the non-linear relationships and spatial heterogeneity between regional-scale production and harvested area. This comparison implies that the identifiable information contained in the embeddings requires stronger function approximation capacity to be stably exploited, and deep architectures are more suitable under this input setting.

Method	Total Production		Harvested Area		Time (min)	
	R^2	RMSE (kg)	R^2	RMSE (ha)	Train	Test
XGBoost Regressor	0.65	48,868.57	0.66	22.54	0.35	<0.01
RepViT	0.69	48,282.79	0.63	23.49	27.85	0.31
ResNet-152	0.76	42,084.41	0.75	20.33	30.08	0.32
ConvNeXt V2	0.76	42,117.30	0.79	18.78	28.53	0.37
Proposed Y-Net	**0.73**	**43,049.71**	**0.75**	**19.34**	**23.85**	**0.28**

Table 3: Baseline comparison on the test set in real space. We report R^2 and RMSE for total production and harvested area, along with training and inference time.

Across deep models, the results highlight a clear accuracy-efficiency trade-off driven by architecture choices. Among the transformer-style baseline in this table, RepViT shows weaker performance on both targets (production R^2=0.69 , area R^2=0.63), indicating that, under the same embedding input, its representation and regression capacity is less effective for regional production elements than the proposed design. In contrast, the proposed Y-Net achieves higher accuracy (production R^2=0.73 , area R^2=0.75) while maintaining comparable inference cost (0.28 vs. 0.31,min), demonstrating that the structured dual-head design provides a more favourable solution than the RepViT alternative in this setting.

Heavier CNN backbones achieve the highest accuracy in this comparison. ResNet-152 reaches production R^2=0.76 and area R^2=0.75, while ConvNeXt V2 further improves to production R^2=0.76 and area R^2=0.79. Y-Net is slightly below these two models on R^2, but it remains within a close performance regime and yields competitive absolute errors. This supports the intended non-inferiority interpretation of the baseline study: the proposed model provides reliable main-task estimates without relying on the largest-capacity backbones.

The runtime comparison further differentiates Y-Net in terms of deployability. Y-Net reduces training time to 23.85 min, compared with 30.08 min for ResNet-152 and 28.53 min for ConvNeXt V2, and also attains the fastest inference time among deep models in the table (0.28 min). While these differences may appear moderate on the benchmark setting, they become operationally significant when scaling to regional monitoring workflows.

To give a rough sense of the magnitude, we provide a linear extrapolation based on the training setup. Our current training uses 5,000 samples, each covering 1.28×1.28 km^2 (i.e., 1.6384 km^2 per sample), corresponding to ~ 8,192 km^2 in total. Scaling to the

Northeast China region (1.24×10^6 km^2) implies a factor of ~ 151× more spatial coverage. Under a linear-time assumption, the estimated training time would increase from 23.85 min to ~ 3,610 min (~ 60.2 h) for Y-Net, versus ~ 4,555 min (~ 75.9 h) for ResNet-152 and ~ 4,318 min (~ 72.0 h) for ConvNeXt V2. This corresponds to savings of roughly 15.8 h relative to ResNet-152 and 11.8 h relative to ConvNeXt V2 for a single training run, and the gap would further accumulate across multi-year retraining and repeated updates.

Therefore, the proposed Y-Net offers a practical accuracy–cost balance: it is more accurate than the RepViT baseline, close to the strongest CNN backbones, and substantially more efficient in training and inference, which makes it a reliable and scalable backbone for the overall framework, especially when integrating additional modules such as physical consistency and evidence-driven interpretation.

It should be noted that this study does not deny that larger backbones may achieve higher R^2 under certain data distributions. However, the gains shown in table 3 are relatively limited and come with higher computational costs. Given the research goal of this work, Y-Net is positioned as the basic prediction module of an extensible framework: while meeting the non-inferiority requirement on the main tasks, it prioritizes training and inference efficiency to support sustainable operation in modular expansion and cross-region applications.

4.3.2 Model Performance under Incomplete Supervision

Table 4 shows that the three configurations achieve production prediction performance within the same range. Even when both harvested area supervision and climate-related supervision are completely missing, “Production-only” still reaches R^2=0.71 with RMSE =43,828.75 kg, indicating that the model can be trained stably and produce usable outputs when it relies only on the core production labels. After introducing harvested area supervision (Production + Area (w/o climate)), the production metrics remain in a similar range (R^2=0.73, RMSE =43,592.48 kg), which suggests that adding an area head does not impose a clear burden on the main task, while it provides area estimation capability. After further adding climate-related components (Proposed), the production RMSE decreases to 43,049.71 kg, but the overall difference remains small; area prediction is also stable (R^2=0.75, RMSE =19.34 ha). These results support the systematic design choices of this work: the area head and the climate components are plug-and-play modules. Their inclusion does not change the effectiveness boundary of the main tasks, which allows the framework to be configured according to supervision availability. As a result, it can maintain core production estimation ability under incomplete supervision, and when data conditions allow, it can extend outputs and the evidence layer to support the subsequent explanatory closed loop.

Method	Total Production		Harvested Area	
	R^2	RMSE (kg)	R^2	RMSE (ha)
Production-only	0.71	43,828.75	–	–
Production + Area (w/o climate)	0.73	43,592.48	0.76	20.51
Proposed	**0.73**	**43,049.71**	**0.75**	**19.34**

Table 4: Ablation study under incomplete supervision settings. "Production-only" uses total production labels only; "Production + Area (w/o climate)" uses total production and harvested area labels but disables the climate component; "Proposed" is the full model.

4.3.3 Temporal Generalization Performance (LOYO)

The results of the Generalization Ability Analysis are shown in table 5. The statistics show that under LOYO testing, the average coefficient of determination (Avg R^2) is 0.5800, which is lower than the result under a random split test set ($R^2 \approx 0.73$). This performance drop is within expectation and reflects the inherent challenge of temporal domain shift in agricultural data, i.e., distribution differences across years caused by climate fluctuations, variety replacement, and changes in management practices. Even so, an average R^2 of 0.58 indicates that the model has learned yield-related features that generalize across years, rather than only memorizing over fitted noise from specific years.

Test Year	Total Production		Harvested Area	
	R^2	RMSE (kg)	R^2	RMSE (ha)
2019	0.5981	58,858.28	0.6009	24.86
2020	0.6512	49,803.07	0.6569	23.50
2021	0.5976	44,186.91	0.5881	20.39
2022	0.5755	45,440.62	0.6738	19.25
2023	0.5175	62,472.67	0.5257	26.77
Average	**0.5800**	**52,152.31**	**0.5831**	**24.16**

Table 5: Temporal generalization performance evaluated using a Leave-One-Year-Out (LOYO) strategy. The model was trained on four years of data and tested on the remaining target year to assess robustness against inter-annual variability.

From year to year, the model shows relatively stable performance from 2019 to 2022. Among them, 2020 achieves the highest prediction accuracy (Total R^2=0.6512). This may be because the climate in Northeast China was relatively stable in that year, and soybean growth features were more typical, making them easier for AEF visual encoding to capture. However, the model performance drops obviously in 2023 (Total R^2=0.5175, Area R^2=0.5257). A closer look at meteorological records suggests that Northeast China experienced relatively rare extreme events in 2023 (https://www.cma.gov.cn/zfxxgk/gknr/qxbg/202402/t20240223_6084527.html), which caused large deviations in surface spectral features compared with previous years (out-of-distribution, OOD). Since the training set (2019–2022) lacks samples with such extreme feature distributions, the model shows a generalization bottleneck when facing the abnormal features in 2023.

It is also worth noting that the prediction accuracy for harvested area reaches a peak in 2022 (R^2=0.6738), but drops sharply to 0.5257 in 2023. This strong fluctuation indicates that extreme weather can disturb the judgment of harvest ability: in severely affected years, many fields that were planted with soybean may show textures similar to bare soil or weeds due to crop failure, which makes it difficult for the model to define accurate harvested boundaries.

In summary, SHiPA-LLM demonstrates reliable temporal transferability in normal years, but it still faces challenges when encountering unseen extreme anomaly years. This further highlights the importance of introducing the environmental perception branch in this study, which can help identify the applicability boundary of the model by monitoring meteorological anomalies.

4.4 Attribution Differences of Agronomic RAG Tool under Knowledge Augmentation

To evaluate how the agricultural knowledge base influences the reasoning behaviour of the large language model, this study uses the same cases and compares the generated reports under two modes: Without Database and With Database. For ease of presentation, figure 8 presents one low-yield case and analyses the differences in processing depth between the two modes from four aspects: overview style, diagnosis logic, evidence usage, and recommended actions.

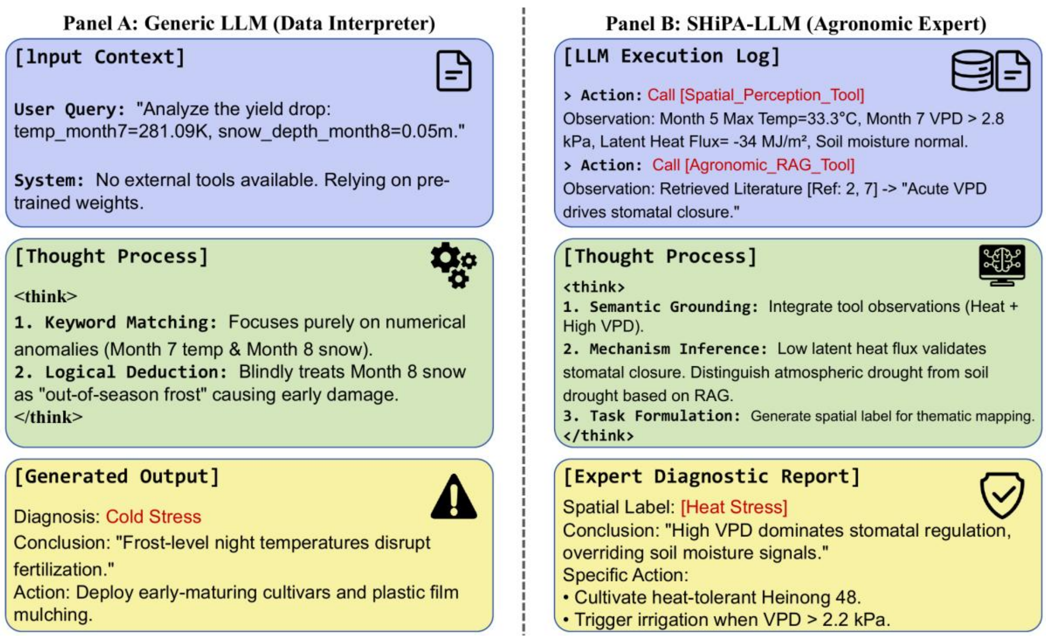

Figure 8: Example of SHiPA-LLM attribution with evidence grounding for a 2020 case field at 43.7126° N, 118.1983° E in eastern Inner Mongolia, Northeast China. The agent uses tool-selected production estimates, derived yield, monthly meteorological factors, and retrieved agronomic knowledge to produce a stressor diagnosis.

4.4.1 Divergence in Diagnosis Logic and Indicator Focus

In the core diagnosis logic, introducing the knowledge base leads the model to focus on different dimensions of meteorological features, and therefore produces different attribution paths.

The Without Database mode follows a linear association logic and mainly focuses on statistical means and explicit signals. Based on a lower monthly mean temperature in July ($281.1\ \mathrm{K}$ and an abnormal snow depth in August ($>0.05\ \mathrm{m}$), it concentrates on the possible suppression of reproductive growth by low temperature, and reaches a diagnosis of cold stress.

The With Database mode shows more attention to combined physiological mechanisms. It does not limit itself to monthly mean temperature, but instead identifies the extreme maximum temperature in May ($33.3^{\circ}\ \mathrm{C}$) and a derived indicator, vapour pressure deficit (VPD $>2.8\ \mathrm{kPa}$). This mode interprets a low latent heat flux as a physiological signal of stomatal closure, and argues that high VPD dominates water regulation processes. It therefore concludes heat stress. This indicates that the knowledge base guides the model to shift from single-factor analysis to multi-factor integrated analysis.

4.4.2 Depth of Evidence Chain and Literature Support

The Without Database mode mainly relies on listing raw monitoring variables, such as directly citing specific predicted temperature values and leaf area index (LAI). However, it does not expand the underlying mechanisms behind these data, and it does not cite external literature.

The With Database mode builds a composite evidence chain that combines derived indicators and academic literature. It not only computes indicators with clear physical meaning, such as VPD and latent heat flux, but also explicitly cites specific references (e.g., ref2,ref7) to support response patterns of pollen viability and stomatal behaviour under certain meteorological conditions (e.g., high VPD). This citation mechanism distinguishes the subtle difference between atmospheric drought and soil drought, and strengthens the theoretical depth of the reasoning process.

4.4.3 Fineness of Recommendations

The Without Database mode, based on a cold-stress logic, provides general adaptation strategies, including using plastic film mulching to increase soil temperature, planting cold-tolerant and early-maturing varieties, and adjusting sowing dates based on risk.

The With Database mode, based on heat stress and VPD stress, proposes mechanism-specific actions. The recommendations include selecting specific heat-tolerant varieties (e.g., Heinong 48), setting a precise irrigation trigger mechanism based on a VPD threshold (VPD $>2.2\ \mathrm{kPa}$), and adopting strip intercropping to optimize the canopy microclimate.

In summary, figure 8 indicates that introducing the knowledge base not only changes the language style of the model, but more importantly expands the dimensions for interpreting meteorological data. As a result, the model can generate a deeper report that includes derived-indicator analysis, literature support, and specific variety recommendations.

4.5 Monthly Attribution Maps

The monthly attribution maps provide the main spatial attribution result. They show the dominant stressor assigned by the workflow for the lower 25% of test parcels ranked by yield. This subset is used for display because higher-yield parcels are mostly classified as normal condition, which would make the full-map visualization visually sparse and less informative. The maps share one global legend panel for heat stress, drought, waterlogging, cold stress, and normal condition. The ordered maps make the attribution output traceable because users can inspect how parcel-level diagnosis changes over the growing season and across years. The stressor classes follow the directional evidence rules in Table 1.

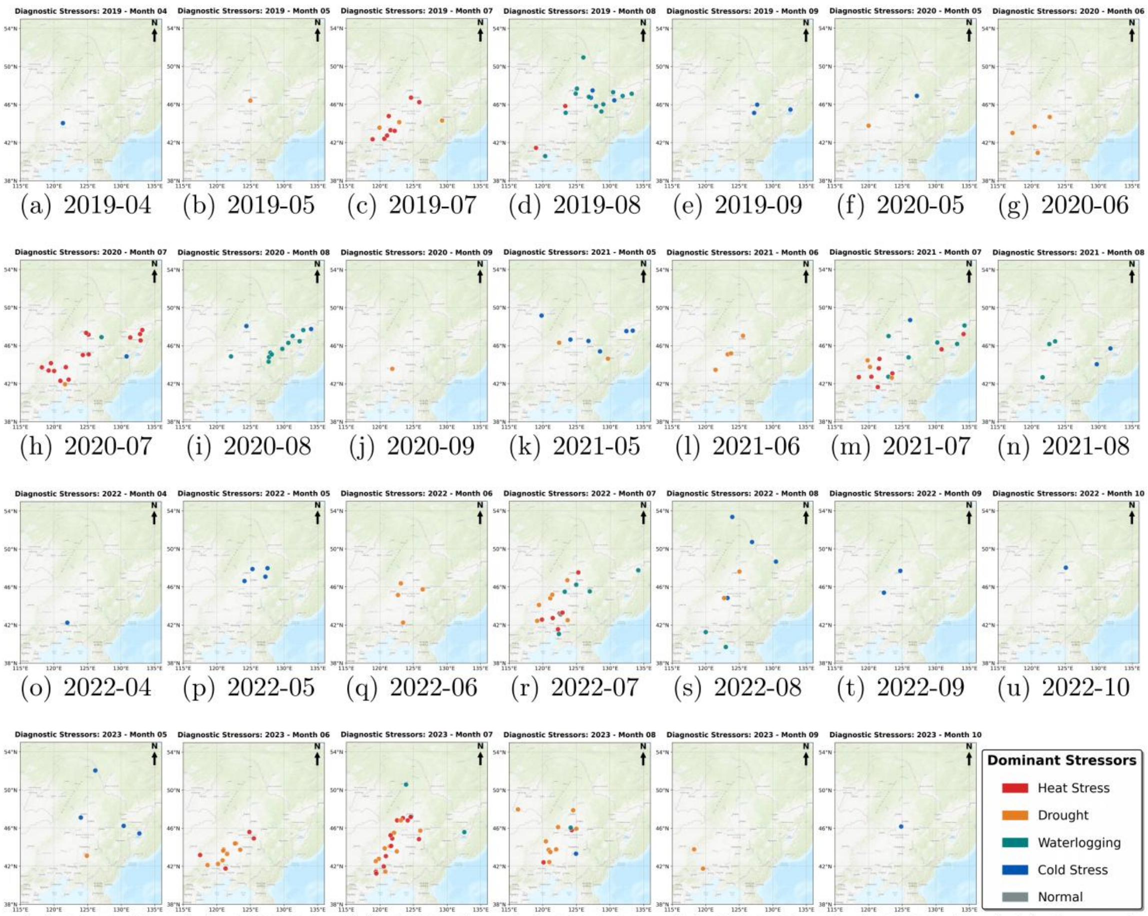

(a) 2019-04 (b) 2019-05 (c) 2019-07 (d) 2019-08 (e) 2019-09 (f) 2020-05 (g) 2020-06
(h) 2020-07 (i) 2020-08 (j) 2020-09 (k) 2021-05 (l) 2021-06 (m) 2021-07 (n) 2021-08
(o) 2022-04 (p) 2022-05 (q) 2022-06 (r) 2022-07 (s) 2022-08 (t) 2022-09 (u) 2022-10
(v) 2023-05 (w) 2023-06 (x) 2023-07 (y) 2023-08 (z) 2023-09 (aa) 2023-10 (ab) Legend

Figure 9: Monthly attribution maps for the lower-yield quartile of the 1,000 test parcels, ordered by year and month. The first 27 panels show the dominant stressor assigned by SHiPA-LLM, and the final panel gives the shared legend for heat stress, drought, waterlogging, cold stress, and normal condition.

Figure. 9 shows a clear seasonal progression in the lower-yield quartile. Early-season panels contain only sparse non-normal labels, mainly cold stress in April–May, and these labels are limited to a small number of parcels. Drought labels become more visible in June, especially in 2020, 2021, 2022, and 2023, and they are repeatedly located in central and western parts of the sampled parcels. July is the main stress month in the sequence. Heat stress dominates or co-dominates the July panels in 2019 and 2020, while 2021–2023 show mixed heat, drought, and waterlogging signals, with 2023 presenting the broadest and densest anomaly pattern. In August, the dominant signal shifts away from a purely heat-driven pattern: 2019 and 2020 show stronger waterlogging clusters, 2021–2022 contain more scattered waterlogging and cold-stress labels, and 2023 keeps a visible drought signal into late summer. September and October panels become sparse again, with isolated drought or cold-stress labels. The repeated central-western heat and drought clusters and the more eastern waterlogging patches form an organized spatial pattern in the lower-yield subset.

5 Discussion

This study develops SHiPA-LLM, a closed-loop agricultural intelligent system that couples geospatial perception with large language model reasoning. Unlike traditional deep learning models that mainly focus on single-task numerical prediction, SHiPA-LLM is designed to build an end-to-end integrated framework from visual feature inputs to agronomic decision outputs. Methodologically, this system does not follow the conventional decoupled path that separately treats harvested area extraction and yield estimation. Instead, it adopts a production-and-area-first strategy. The model first uses single-source AEF embedding features to build a unified latent-space representation of both production states (total production and harvested area) and environmental backgrounds (meteorological variables). It then treats these perception results as immutable factual inputs, integrates them into a structured evidence set, and drives a knowledge-base–augmented large language model to conduct attribution analysis. This design is not only intended to improve prediction accuracy, but also to address a key bottleneck of existing end-to-end models in agricultural monitoring, namely the lack of physical constraints and the lack of mechanism-based interpretability.

5.1 Discussion of the Integrated Closed-loop Design

The core advantage of SHiPA-LLM in this study is that it builds a physics-closed loop from environmental perception to decision support. Unlike traditional deep learning models that focus on a single numerical prediction task, this approach overcomes the inherent limitations of the conventional workflow of multi-source heterogeneity and task decoupling at the system level. It does so by integrating a unified representation at the input end, a physics-coupled estimation process at the computation end, and a cognitively anchored output at the decision end. To systematically justify the effectiveness of this architecture, this section discusses three dimensions: the unified perception foundation (Input), the physics-coupled estimation workflow (Process), and the cognitively anchored attribution mechanism (Output). Together, these three dimensions form the full lifecycle of the system from perception-cognition-action. They represent a shift from stitching heterogeneous data to implicit physics encoding, from decoupled tasks to holistic consistency constraints, and from black-box prediction to an auditable expert system.

5.1.1 Unified Perception Input and Single-source Embeddings

Existing agricultural monitoring systems often rely on a patchwork data strategy to incorporate environmental drivers of crop growth, where multispectral satellite observations are combined with gridded reanalysis products (e.g., ERA5) and ancillary layers such as soil property maps. In regional-scale settings, however, such heterogeneous fusion pipelines are frequently sensitive to spatiotemporal inconsistencies, because the constituent data sources differ in spatial support, temporal sampling, and preprocessing conventions; consequently, resampling, reprojection, and interpolation become unavoidable steps that may introduce alignment uncertainty and smoothing artifacts. (Zhang et al., 2024) analyse this issue in depth in the EarthMarker study, arguing that the semantic gap between image-based remote sensing signals and non-image environmental variables makes naive feature-level concatenation inefficient for transferring environmental semantics, and that forced alignment across heterogeneous grids can propagate interpolation artifacts during preprocessing. Complementarily, (Li et al., 2026) report in the KiwiGuard system that open-ended stacking of multi-modal inputs does not necessarily translate into coherent environmental perception in practice, and may lead to under-utilization of modality-specific information in complex agricultural scenes.

In contrast, SHiPA-LLM adopts AEF embeddings as a unified perceptual foundation, thereby shifting the burden of cross-source integration from downstream task-specific preprocessing to the representation learning stage. Because the AEF foundation model is trained to produce a consistent latent field under irregular, multi-source Earth observation inputs, including gridded reanalysis variables, SHiPA-LLM can operate on a single embedding stream that implicitly carries both visual and environmental information (Brown et al., 2025). Practically, this design reduces the need to explicitly co-register coarse-resolution meteorological grids with high-resolution imagery—an operation that typically requires repeated resampling and reprojection and can accumulate registration uncertainty over large domains. By consuming embeddings that are already harmonized in a shared latent space, SHiPA-LLM avoids treating heterogeneous sources as independently overlaid layers in physical space, thereby mitigating preprocessing-induced artifacts and simplifying the data engineering pipeline. As a result, the model can maintain a more consistent correspondence between visual cues and environmental representations at the feature level, which is particularly desirable for regional-scale estimation and subsequent evidence-grounded attribution.

5.1.2 Joint Estimation of Production And Area

Traditional yield estimation workflows usually treat crop area extraction and yield regression as two decoupled and independent tasks. (Owais et al., 2026) provide an in-depth analysis of this issue in their study on dense-planted crops. They point out that under real field conditions, complex backgrounds and illumination changes can easily cause the target signal to be overwhelmed by non-crop noise. In such an uncontrolled environment, end-to-end models without physical constraints struggle to distinguish between two essentially different states: poor crop growth and low crop proportion within a pixel. This kind of blind regression not only tends to produce physical paradoxes at the regional scale (e.g., high yield predicted where no crop is planted), but also makes the prediction variance uncontrollable in mixed pixels, thereby reducing the robustness of overall estimation.

To address this problem, SHiPA-LLM adopts a coupled estimation workflow named Production-and-Area-First. It first estimates total production and harvested area, and then derives yield through a physical constraint ($\text{Yield}=P/A$). The non-linear jump of yield accuracy with increasing harvested area proportion reveals an SNR degradation mechanism caused by mixed pixels. Unlike conventional methods that attempt to force numerical fitting on all pixels, this workflow automatically reduces the influence of low-purity marginal parcels through the denominator effect. In essence, this strategy builds a reliability-oriented monitoring mechanism: it outputs high-confidence results in core harvested areas (high SNR), while maintaining physical consistency in fragmented marginal areas (low SNR). As a result, it achieves better error control at the regional statistical scale than end-to-end regression.

5.1.3 Attribution Reasoning Grounded in Evidence and Domain Knowledge

At the output stage, a core challenge for an agricultural intelligent system is how to transform numerical predictions into trustworthy agronomic advice. Although general large language models show strong text generation ability, when strict domain boundaries are missing, they can easily produce attribution narratives that look reasonable but are in fact incorrect. (Yang et al., 2026) clearly point out that even advanced generative frameworks that integrate CNNs and VLMs cannot fully eliminate the risk of hallucinations when facing noisy agricultural environmental data, and they often generate disease diagnoses that do not match image facts. (Xiao and Ma, 2025) also report in the development of ChangeGPT that a general model without domain-specific constraints, when performing integrated analysis, needs an extremely complex tool selection design to keep reasoning logic accurate; otherwise it can fall into false causal inference.

To address this issue, SHiPA-LLM introduces a cognitive grounding mechanism. The system does not rely on free-form generation by the LLM. Instead, it packages the production states and the reconstructed environmental vectors output by the perception module as immutable evidence, and it uses retrieval-augmented generation (RAG) to call a peer-reviewed agronomic knowledge base. This mechanism strictly restricts the reasoning process to the intersection of physical facts and scientific consensus, and thus enables the auditability of attribution reports: each diagnostic conclusion (e.g., heat stress) can be traced back to specific numerical evidence (e.g., VPD $>2.2\ \mathrm{kPa}$) and clear literature sources. This marks a key step for agricultural AI from an uninterpretable black-box prediction toward a logically traceable expert diagnostic system.

5.1.4 Automation for Scalable Monitoring and Diagnosis

Beyond the input-process-output decomposition, an additional practical advantage of SHiPA-LLM lies in its degree of automation. By operating on a single stream of geo-foundation embeddings, the perception module can be trained without handcrafted feature engineering or explicit cross-source alignment. Under the same training procedure, the model learns mappings from embeddings to production factors (total production and harvested area) and also reconstructs environmental variables as a structured evidence package, reducing the manual effort typically required to assemble and harmonize heterogeneous drivers for regional monitoring.

On the decision side, the attribution component further supports crop-aware evaluation. Rather than relying on a fixed driver list, the system leverages the peer-reviewed knowledge base to prioritize agronomically relevant factors and their critical seasonal windows for the target crop, and evaluates them against the reconstructed environmental evidence. This enables the diagnostic report to focus on plausible mechanisms for the given crop and region while keeping each claim traceable to explicit numerical evidence and citations, strengthening the practical usability of the explanation beyond free-form generation. As shown in figure 8, the LLM-based module can automatically identify a compact set of key drivers and their relevant months for the target crop, and ground the selected factors in both retrieved literature and the numerical evidence package.

Taken together, these automation properties complement the efficiency of the proposed prediction backbone. In regional-scale deployments, where inference is repeated over large spatial domains and across years, reductions in data-engineering overhead and per-run computation accumulate at scale. This makes the closed-loop design not only methodologically coherent but also operationally feasible for routine monitoring and diagnosis.

5.2 Applicability and Generalization Boundaries

5.2.1 Mechanisms Behind Performance Variation Under Spatial Heterogeneity

The spatial distribution of model performance shows a clear core production-marginal area structure. In the core regions of the Sanjiang Plain and the Songnen Plain, which are dominated by large state-owned farms, the model achieves very high explanatory power (R^2>0.8). This high confidence mainly comes from the high spectral purity produced by large contiguous monoculture patterns, which allows AEF embeddings to capture clear crop features. In contrast, prediction accuracy drops obviously in the western agro-pastoral transition zone and along the eastern mountainous margins. This spatial non-stationarity is not caused by latitude-related geometric distortion, but by field fragmentation and complex mixed-cropping patterns (e.g., soybean-maize strip intercropping). In these marginal scenes, pixels contain mixed signals from soil, weeds, and non-target crops, which greatly reduces the signal-to-noise ratio in feature space. Therefore, the best applicability domain of this model should be strictly defined as intensive agricultural regions with large-scale planting, and in fragmented marginal lands its outputs should be interpreted together with larger uncertainty intervals.

However, this spatial heterogeneity, matches the optimal engineering property for national-level agricultural monitoring. From the strategic perspective of food security monitoring, core harvested areas contribute most of regional total production. The excellent stability of SHiPA-LLM in these high-yield areas ensures that the main baseline of regional total production estimation remains reliable. In marginal low-yield areas, although point-level predictions may fluctuate, their contribution weight to total production is low, and random errors can be statistically cancelled during regional aggregation (error cancellation). Therefore, they do not cause substantial impacts on the final provincial- or national-level production estimates. This demonstrates the robustness and reliability of the system for large-scale operational applications under complex land-surface environments.

5.2.2 Cross-year Degradation and Domain Shift Risk

The cross-year LOYO evaluation exposes the vulnerability of the model when facing temporal domain shift. Although the model remains stable in climate-normal years from 2019 to 2022 ($R^2 \approx 0.6$), it shows a clear performance degradation in 2023 (with R^2 dropping near 0.5). This failure mode is closely related to extreme flooding and reduced sunshine events in Northeast China in 2023. From a machine learning perspective, extreme climate events cause crop growth features to deviate from the statistical distribution of historical training data, forming typical out-of-distribution (OOD) samples. The current static embedding representation mainly relies on historical experience to build the mapping between feature and production. When it encounters unseen disaster features, the model's inference ability is suppressed. This finding highlights the limitation of relying only on static spatial features, and suggests that future system development must include uncertainty quantification mechanisms, so that low-confidence warnings can be automatically triggered when OOD samples occur.

5.2.3 Limits of Environmental Reconstruction and Interpretability

The differences in environmental internalization results further define the identifiability boundary of single-source perception. The model can reconstruct temperature ($R^2 \approx 0.99$) and other accumulated variables such as precipitation with high accuracy because these variables have long-term integrated effects on crop growth. Their biological imprints (e.g., plant height and canopy closure) are observable state variables in static imagery. However, for instantaneous flux variables such as evaporation, the reconstruction ability is extremely weak. This is because instantaneous fluxes are controlled by high-frequency dynamic factors such as wind speed and stomatal conductance, and these rate variables cannot be captured effectively by annual static snapshots. Therefore, in attribution analysis, the explanatory power of SHiPA-LLM is mainly limited to climate-scale cumulative stresses (e.g., insufficient accumulated temperature and drought), and it is not suitable for explaining yield fluctuations caused by short-term weather processes (e.g., lodging due to strong wind and hail). Clarifying this physical boundary helps ensure the scientific rigour of subsequent attribution narratives.

5.2.4 Data Scale and Computational Resource Constraints

In this study, we select about 5,000 samples for training and about 1,000 samples for testing, mainly due to computational resources and the storage/compute cost brought by data scale. The original imagery has a spatial resolution of 10 m and contains 64 bands, and the covered region is about 1.24×10^6 km^2. Even under the current sample size, data I/O and feature computation have already reached the GB scale. If we further include all pixel-level data over the full region for training and testing, the data volume would quickly grow to the TB or even PB level, which would clearly exceed the capacity of common computing platforms. Under this practical constraint, we adopt a sampling-based training strategy, and we do not continue expanding the sample size after the model reaches R^2>0.70 on the validation set, in order to control experimental cost and ensure iteration efficiency. It is worth noting that even with a relatively limited number of samples, the model has already achieved stable and usable estimation accuracy. With stronger computing resources and larger-scale training data in the future, it is reasonable to expect further performance improvements.

5.3 Future Work and System Extensions

Based on our analysis of the applicability boundaries and failure modes, SHiPA-LLM can be further improved in the following directions. First, to address spatial non-stationarity caused by fragmented fields and mixed-cropping marginal areas, explicit uncertainty quantification and a reliability reporting mechanism should be introduced. In this way, outputs under low-SNR scenes can be presented as confidence intervals or risk warnings, rather than only point estimates. Second, the cross-year LOYO results indicate clear vulnerability to domain shift in extreme anomaly years. In the future, the system should include OOD detection and an automatic warning mechanism, so that conservative reasoning or human-machine collaborative review can be triggered when disaster-related features appear and deviate from historical distributions. Third, environmental variable reconstruction shows that the model has strong identifiability for climate-scale cumulative stresses such as temperature and precipitation, but limited ability for instantaneous flux variables such as evaporation. Therefore, future work can explore time-aware representations (e.g., growing-season or multi-temporal embeddings) and incorporate higher-frequency observations to improve the explanatory power for short-term processes. Finally, systematic validation across more crops and regions is needed to evaluate framework transferability, and to refine the crop-agnostic framework design under different management regimes and phenological differences.

Meanwhile, for future work, although the current focus of this study is to build a knowledge-constrained large language model (LLM) for interpretable regional production estimation and driver attribution, our framework naturally has the potential to evolve toward an agent form. Specifically, based on the current pipeline of multi-factor estimation-evidence retrieval-structured report generation, future work can introduce task planning, tool calling, and closed-loop feedback mechanisms, and thus form an autonomous analysis workflow for agricultural operations. The agent can automatically propose hypotheses from monitoring results (e.g., drought stress, abnormal sowing dates, or insufficient management), and then trigger targeted evidence retrieval and data verification (for example, calling environmental statistics with different time windows, zonal aggregation, threshold filtering, and uncertainty assessment). When conflicts are found or evidence is insufficient, it can adaptively adjust its retrieval strategy and explanation path. Through this iterative reasoning cycle of propose-retrieve-verify-revise, the agent can not only output one-shot attribution conclusions, but also produce auditable analysis chains and action recommendations (e.g., irrigation, replanting, field management, and risk warnings), thereby better supporting regional-scale production decisions and continuous monitoring scenarios.

6 Conclusion

To address the interwoven challenges of costly multi-source data alignment, physical inconsistency in decoupled yield estimations, and the lack of auditable mechanism explanations in large-scale agricultural monitoring, this study develops the SHiPA-LLM framework. Moving away from traditional fragmented workflows, we exploit the high-dimensional feature potential of a single-source geo-foundation model (AlphaEarth) to drive a physics-aware Y-Net. This production-and-area-first strategy effectively mitigates spatial error accumulation, achieving robust regional-scale estimations for soybean in Northeast China with R^2 values of 0.7287 and 0.7482 for total production and harvested area, respectively, while the physics-derived yield accuracy reaches an R^2 of 0.63 under high-purity thresholds. Beyond numerical prediction, the system successfully transforms these quantitative states and reconstructed meteorological variables into trustworthy diagnostic reports via a retrieval-augmented generation (RAG) mechanism, significantly reducing hallucination risks by anchoring the large language model's reasoning in peer-reviewed agronomic literature. Theoretically, this framework demonstrates a paradigm shift from complex multi-source data stitching to implicit representation learning, and from black-box prediction to an auditable, evidence-driven expert system. Practically, it offers a highly automated, low-cost solution for regional food security monitoring, disaster damage assessment, and operational decision-making. Consequently, future work will focus on integrating OOD detection, few-shot learning, and online adaptation mechanisms to further enhance the framework's generalization ability and decision-support value in open, dynamic environments.

Declaration of competing interest

The authors declare that they have no known competing financial interests or personal relationships that could have appeared to influence the work reported in this study.

Data availability

The data supporting the findings of this study are openly available on Zenodo at https://doi.org/10.5281/zenodo.21791492.

CRediT authorship contribution statement

Heyan Di: Conceptualization, Methodology, Software, Investigation, Formal analysis, Visualization, Writing - original draft, Writing - review & editing. **Yachao Zhao:** Conceptualization, Methodology, Writing - review & editing. **Jiaojiao Tian:** Data curation, Writing - review & editing. **Xin Du:** Conceptualization, Methodology, Supervision, Project administration, Funding acquisition, Writing - review & editing.

Qiangzi Li: Supervision, Funding acquisition. **Yuan Zhang:** Validation, Writing - review & editing. **Hongyan Wang:** Resources, Supervision. **Jiansong Luo:** Data curation, Validation.

Funding statement

This study was supported by the National Key R&D Program of China (2021YFD1500103), National Science Foundation of China (42371359), and Beijing Natural Science Foundation (L251051).

References

Arslan, M., Ghanem, H., Munawar, S., Cruz, C., 2024. A survey on RAG with LLMs. Procedia computer science 246, 3781–3790.

Brown, C.F., Kazmierski, M.R., Pasquarella, V.J., Rucklidge, W.J., Samsikova, M., Zhang, C., Shelhamer, E., Lahera, E., Wiles, O., Ilyushchenko, S., et al., 2025. Alphaearth foundations: An embedding field model for accurate and efficient global mapping from sparse label data. arXiv preprint arXiv:2507.22291.

Chen, T., 2016. XGBoost: A scalable tree boosting system. Cornell University.

De Vos, K., Gebruers, S., Degerickx, J., Iordache, M.-D., Keune, J., Di Giuseppe, F., Pereira, F.V., Wouters, H., Swinnen, E., Van Rossum, K., et al., 2025. Predicting below-average NDVI anomalies for agricultural drought impact forecasting. Remote Sensing of Environment 330, 114980.

Giller, K.E., Delaune, T., Silva, J.V., Descheemaeker, K., Van De Ven, G., Schut, A.G., Van Wijk, M., Hammond, J., Hochman, Z., Taulya, G., et al., 2021. The future of farming: Who will produce our food? Food Security 13, 1073–1099.

Guo, F., Wang, P., Tansey, K., Zhang, Y., Li, M., Liu, J., Zhang, S., 2024. A novel transformer-based neural network under model interpretability for improving wheat yield estimation using remotely sensed multi-variables. Computers and Electronics in Agriculture 223, 109111.

Hartman, G.L., West, E.D., Herman, T.K., 2011. Crops that feed the world 2. Soybean—worldwide production, use, and constraints caused by pathogens and pests. Food Security 3, 5–17.

He, K., Zhang, X., Ren, S., Sun, J., 2016. Deep residual learning for image recognition, in: Proceedings of the IEEE Conference on Computer Vision and Pattern Recognition. pp. 770–778.

Islam, M.R., Ahmed, M.U., Barua, S., Begum, S., 2022. A systematic review of explainable artificial intelligence in terms of different application domains and tasks. Applied Sciences 12, 1353.

Jones, E.J., Bishop, T.F., Malone, B.P., Hulme, P.J., Whelan, B.M., Filippi, P., 2022. Identifying causes of crop yield variability with interpretive machine learning. Computers and electronics in agriculture 192, 106632.

Kasampalis, D.A., Alexandridis, T.K., Deva, C., Challinor, A., Moshou, D., Zalidis, G., 2018. Contribution of remote sensing on crop models: A review. Journal of Imaging 4, 52.

Keating, B.A., Carberry, P.S., Hammer, G.L., Probert, M.E., Robertson, M.J., Holzworth, D., Huth, N.I., Hargreaves, J.N., Meinke, H., Hochman, Z., et al., 2003. An overview of APSIM, a model designed for farming systems simulation. European journal of agronomy 18, 267–288.

Kendall, A., Gal, Y., Cipolla, R., 2018. Multi-task learning using uncertainty to weigh losses for scene geometry and semantics, in: Proceedings of the IEEE Conference on Computer Vision and Pattern Recognition. pp. 7482–7491.

Li, Q., Zhang, Y., Mai, Z., Chen, Y., Lou, S., Huang, H., Zhang, J., Zhang, Z., Wen, Y., Li, W., et al., 2025. Can large multimodal models understand agricultural scenes? Benchmarking with AgroMind. arXiv preprint arXiv:2505.12207.

Li, X., Yang, S., Li, S., 2026. From identification to prevention: A kiwi disease diagnosis system integrating vision and large language models. Computers and Electronics in Agriculture 244, 111484.

Ma, Y., Liang, S.-Z., Myers, D.B., Swatantran, A., Lobell, D.B., 2024. Subfield-level crop yield mapping without ground truth data: A scale transfer framework. Remote sensing of environment 315, 114427.

Ma, Y., Zhang, Z., Kang, Y., Özdoğan, M., 2021. Corn yield prediction and uncertainty analysis based on remotely sensed variables using a bayesian neural network approach. Remote Sensing of Environment 259, 112408.

Mena, F., Pathak, D., Najjar, H., Sanchez, C., Helber, P., Bischke, B., Habelitz, P., Miranda, M., Siddamsetty, J., Nuske, M., et al., 2025. Adaptive fusion of multi-modal remote sensing data for optimal sub-field crop yield prediction. Remote Sensing of Environment 318, 114547.

Owais, M., Fahmy, I., Seneviratne, L., Hussain, I., 2026. SAMConvFormer+ LLM: Exploring synergistic fusion of segment anything model with joint convolutional transformer and large language model to advance dense agricultural crop analysis. Computers and Electronics in Agriculture 240, 111192.

Qin, X., Wu, B., Zhang, M., Wu, F., Li, M., Zeng, H., Tian, F., 2026. High-frequency, real-time parcel-level agricultural monitoring framework: Integrating tower-based cameras and artificial intelligence. Computers and Electronics in Agriculture 240, 111153.

Sabater, M., 2019. ERA5-land monthly averaged data from 1981 to present, copernicus climate change service (C3S) climate data store (CDS). Earth Syst. Sci. Data 55, 5679.

Sodhi, M.S., Tang, C.S., 2021. Supply chain management for extreme conditions: Research opportunities. Journal of Supply Chain Management 57, 7–16.

Stiller, S., Grahmann, K., Ghazaryan, G., Ryo, M., 2024. Improving spatial transferability of deep learning models for small-field crop yield prediction. ISPRS open journal of photogrammetry and remote sensing 12, 100064.

Van Diepen, C. van, Wolf, J. van, Van Keulen, H., Rappoldt, C., 1989. WOFOST: A simulation model of crop production. Soil use and management 5, 16–24.

Vogel, E., Donat, M.G., Alexander, L.V., Meinshausen, M., Ray, D.K., Karoly, D., Meinshausen, N., Frieler, K., 2019. The effects of climate extremes on global agricultural yields. Environmental Research Letters 14, 054010.

Wang, A., Chen, H., Lin, Z., Han, J., Ding, G., 2024. Repvit: Revisiting mobile cnn from vit perspective, in: Proceedings of the IEEE/CVF Conference on Computer Vision and Pattern Recognition. pp. 15909–15920.

Wang, A.X., Tran, C., Desai, N., Lobell, D., Ermon, S., 2018. Deep transfer learning for crop yield prediction with remote sensing data, in: Proceedings of the 1st ACM SIGCAS Conference on Computing and Sustainable Societies. pp. 1–5.

Wang, C., Chen, Y., Tong, W., Zhou, W., Li, J., Xu, B., Hu, Q., 2023. Mapping crop phenophases in reproductive growth period by satellite solar-induced chlorophyll fluorescence: A case study in mid-temperate zone in china. ISPRS Journal of Photogrammetry and Remote Sensing 205, 191–205.

Woo, S., Debnath, S., Hu, R., Chen, X., Liu, Z., Kweon, I.S., Xie, S., 2023. Convnext v2: Co-designing and scaling convnets with masked autoencoders, in: Proceedings of the IEEE/CVF Conference on Computer Vision and Pattern Recognition. pp. 16133–16142.

Wu, H., Mu, W., Zhong, D., Du, Z., Li, H., Tao, C., 2025. FarmSeg_VLM: A farmland remote sensing image segmentation method considering vision-language alignment. ISPRS Journal of Photogrammetry and Remote Sensing 225, 423–439.

Xiao, Z., Ma, J., 2025. LLM agent framework for intelligent change analysis in urban environment using remote sensing imagery. Automation in Construction 177, 106341.

Xiong, X., Zhong, R., Tian, Q., Huang, J., Zhu, L., Yang, Y., Lin, T., 2024. Daily DeepCropNet: A hierarchical deep learning approach with daily time series of vegetation indices and climatic variables for corn yield estimation. ISPRS Journal of Photogrammetry and Remote Sensing 209, 249–264.

Xu, J., Du, X., Dong, T., Li, Q., Zhang, Y., Wang, H., Xiao, J., Zhang, J., Shen, Y., Dong, Y., 2026. NortheastChinaSoybeanYield20m: An annual soybean yield dataset at 20 m in northeast china from 2019 to 2023. Earth System Science Data 18, 2413–2441. https://doi.org/10.5194/essd-18-2413-2026

Yang, S., Guo, J., Yu, J., 2026. A generative AI-driven framework integrating CNN-VLM-LLM for intelligent crop disease diagnosis and control strategy generation. Computers and Electronics in Agriculture 244, 111475.

Yang, Y., Anderson, M.C., Gao, F., Johnson, D.M., Yang, Y., Sun, L., Dulaney, W., Hain, C.R., Otkin, J.A., Prueger, J., et al., 2021. Phenological corrections to a field-scale, ET-based crop stress indicator: An application to yield forecasting across the US corn belt. Remote Sensing of Environment 257, 112337.

Zhang, W., Cai, M., Zhang, T., Zhuang, Y., Li, J., Mao, X., 2024. Earthmarker: A visual prompting multi-modal large language model for remote sensing. IEEE Transactions on Geoscience and Remote Sensing.